Defence Research and Development Canada | Recherche et développement pour la défense Canada

CAN UNCLASSIFIED

The Empirical Canadian High Arctic Ionospheric Model (E-CHAIM)

NmF2 and hmF2

David R. Themens
P.T. Jayachandran
Anthony M. McCaffrey
Benjamin Reid
University of New Brunswick

Prepared by:
University of New Brunswick
3 Bailey Drive
P.O. Box 4400
Fredericton, New Brunswick
Canada
E3B 5A3

PSPC Contract Number: W7714-186507/001/SS
Technical Authority: Thayananthan (Thaya) Thayaparan, Defence Scientist.

Contractor's date of publication: January 2018

Defence Research and Development Canada
Contract Report
DRDC-RDDC-2018-C195
January 2019

CAN UNCLASSIFIED

Canada

IMPORTANT INFORMATIVE STATEMENTS

This document was reviewed for Controlled Goods by Defence Research and Development Canada using the Schedule to the *Defence Production Act*.

The following work is supported through the All Domain Situational Awareness (ADSA) Science & Technology program, contract number W7714-186507/001/SS.

Abstract

We present here the Empirical Canadian High Arctic Ionospheric Model (E-CHAIM) quiet NmF2, perturbation NmF2, and quiet hmF2 models. These models provide peak ionospheric characteristics for a domain above 50°N geomagnetic latitude. Model fitting is undertaken using all available ionosonde and radio occultation electron density data, constituting a dataset of over 28 million observations. A comprehensive validation of the model is undertaken and performance is compared to that of the International Reference Ionosphere (IRI).

In the case of the quiet NmF2 model, the E-CHAIM model provides a systematic improvement over the IRI URSI maps. At all stations within the polar cap, we see drastic RMS error improvements over the IRI by up to 1.3MHz in critical frequency (up to 60% in NmF2). These improvements occur primarily during equinox periods and at low solar activities, decreasing somewhat as one tends to lower latitudes. Qualitatively, the E-CHAIM is capable of representing auroral enhancements in NmF2, as well as the location and extent of the Main Ionospheric Trough (MIT), not reproduced by the IRI. The included NmF2 storm model demonstrates improvements over the IRI by up to 35% and over the quiet-time E-CHAIM model by up to 30%.

In terms of hmF2, over the validation periods used in this study, we found overall RMS errors of ~13km for E-CHAIM, with IRI2007 overall hmF2 errors ranging between 16km and 22km. The E-CHAIM performs comparably to or slightly better than the IRI within the polar cap; however, significant improvements are found within the auroral oval.

Significance for Defence and Security

Initial explorations of OTHR system characteristics, like those of Thayaparan et al. (2016), Saverino et al. (2013), and Cacciamano et al. (2009), have relied on the International Reference Ionosphere (IRI) model for their assessments; however, given the significant issues with IRI performance at high latitudes (e.g. Themens et al. 2014, 2016), one cannot be confident in the resulting assessments of appropriate system frequencies or elevation angles. For example, 70% errors in IRI peak electron density and inverted diurnal variability of the M3000F2 propagation factor, cited in Themens et al. (2014), could result in similar 70% errors in frequency band predictions using this model. The up to 80km errors in peak height can similarly lead to errors in slant range prediction of nearly 200km. Referring to the results of Thayaparan et al. (2016), these errors would place the real predicted frequency band to be completely outside of the range predicted in that study.

With the model developed in this work, we have demonstrated significant improvement over the current standard (the IRI) in the characterization of the critical frequency of the ionosphere within the Canadian polar cap and Auroral Oval. Regarding the peak height of the ionosphere, this model notes considerable improvement over the IRI, particularly within the Auroral Oval during nighttime periods. Both of these improvements should substantially increase the accuracy of OTHR operational domain and frequency band simulations.

Résumé

[**What to do in this section**: Insert translated abstract here.]

[What you need to know: The translation process will be managed the Editorial Board.]

Importance pour la défense et la sécurité

[**What to do in this section**: Insert translated significance text here.]

[What you need to know: The translation process will be managed the Editorial Board.]

Table of contents

List of figures

List of tables

No table of figures entries found.

Acknowledgements

Infrastructure funding for CHAIN was provided by the Canadian Foundation for Innovation and the New Brunswick Innovation Foundation. Science funding is provided by the Natural Sciences and Engineering Research Council of Canada. The authors would like to thank the many ionosonde operators who provided data to this project. This paper uses ionospheric data from the USAF NEXION Digisonde network, the NEXION Program Manager is Mark Leahy. This publication makes use of data from the Qaanaaq and Nord ionosondes, owned by the U.S. Air Force Research Laboratory Space Vehicles Directorate and supported in part by the Air Force Office of Scientific Research. The authors thank Svend Erik Ascanius of the Danish Meteorological Institute and Denmark's Arctic Command for the operation of these ionosondes. This paper uses data from the Juliusruh Ionosonde which is owned by the Leibniz Institute of Atmospheric Physics Kuehlungsborn. The responsible Operations Manager is Jens Mielich. The authors are grateful to Konstantin Ratovski for the operation of the Irkutsk ionosonde. The Tromsø ionosonde is funded in part by QinetiQ. We would also like to thank Dr. Ivan Galkin for his contribution toward integrating the E-CHAIM models into the realtime IRI model (IRTAM).

1 Introduction

It is well known that the high latitude ionosphere poses significant challenges for empirical modelling through its highly dynamic nature, via coupling with the interplanetary magnetic field, and the scarcity, and traditionally difficult processing, of data in these regions [Moskaleva and Zaalov, 2013]. International standards, such as the International Reference Ionosphere (IRI), have been repeatedly shown to perform poorly at high latitudes [Bilitza and Reinisch, 2008]. In Xiong et al. [2013], the IRI was demonstrate to perform poorly in sub-auroral regions, as compared to CHAMP and GRACE satellite in situ and K-Band Ranging measurements, respectively. In Themens and Jayachandran [2016], it was demonstrated that the IRI performs poorly in representing total electron content (TEC) in the Polar Cap, Auroral Oval, and Sub-Auroral regions, particularly during the equinoxes at high solar activity. These issues at high solar activity were also confirmed via Incoherent Scatter Radar (ISR) observations by Bjoland et al. [2016]. Themens et al. [2014] showed that the IRI produces significant errors in its representation of the F2 peak of the ionosphere at high latitudes, including in its representation of the topside thickness, bottomside thickness, peak electron density (NmF2), and peak height (hmF2).

These issues are, however, not solely limited to the IRI. Themens et al. [2013] demonstrated that the sparsity of data in high latitude regions contributes to significant errors in the representation of TEC in these regions by global TEC maps and Themens et al. [2015] showed that the strong gradients in TEC at high latitudes significantly degrade the performance of standard Global Positioning System (GPS)-based TEC calibration techniques. Also, Athieno et al. [2015] and [2016] show that standard HF communications models exhibit significant errors at high latitudes, largely due to errors in the URSI and CCIR critical frequency maps, which are also used in the IRI. All of these studies highlight the need for a new representation of the high latitude ionosphere. To meet this need, we here present the first phase of the Empirical Canadian High Arctic Ionospheric Model (E-CHAIM), which pertains to the representation of NmF2 and hmF2.

Since the creation of the IRI, and similarly the NeQuick [Nava et al., 2008], electron density models, a plethora of data have become available for use in empirical modeling, namely that from new ionosonde and Incoherent Scatter Radar (ISR) deployments in the arctic regions and from radio occultation (RO)-based electron density inversion. These new data sources allow for the modeling of spatial scales that were not available to previous models, and satellite data, in particular, promise to improve the representation of the ionosphere in regions of sparse ground instrument coverage, such as in the arctic regions and over the oceans.

There have been several attempts to create global alternatives to the IRI, some of which were sufficiently successful to warrant their inclusion in the IRI as direct alternatives or replacements to the original IRI model [Shubin, 2015; Altadill et al., 2013; Altadill et al., 2009; Coïsson et al., 2006]. Coïsson et al. [2006] used topside sounder data to develop the NeQuick topside model, which is now the default topside specification in the IRI, since IRI2007. Altadill et al. [2009] used ionosonde data with a spherical harmonic expansion in local time and modified dip angle to create a new bottomside thickness representation, which was later included in IRI2012. Shubin [2015] used radio occultation, ionosonde, and topside sounder data to create a new global hmF2 model, which is slated to replace the IRI's traditional hmF2 model in IRI2016 [Bilitza et al., 2017]. Other global models include the non-linear models of Hoque and Jakowski [2012] and [2011], which provide hmF2 and NmF2, respectively. All of these models are global

representations that highlight significant progress within the empirical ionospheric modeling community over the past decade; however, their ability to model the high latitude ionosphere is still suspect, particularly due to the lack of high latitude data incorporated into these models during fitting and the tendency for global models to emphasize the representation of the much higher amplitude, equatorial and low latitude ionospheric variabilities. As such, we believe that, particularly for the high latitude region, a regional modeling approach is warranted.

Such regional modeling approaches have been attempted in the past. For example, Karpachev et al. [2016] developed a model of ionospheric critical frequency (foF2) for the Main Ionospheric Trough (MIT) region between 45°N and 75°N and between 40°S and 80° using INTERCOSMOS-19 (IK-19) topside sounder and Challenging Minisatellite Payload (CHAMP) in situ data. Their model demonstrated a consistently better representation of the MIT compared to that generated by the IRI; unfortunately, given the MIT focus of the Karpachev et al. [2016] model, only night time (18 – 06 LT) winter (Nov - Feb) values are provided.

Here, we first introduce the general structure of the E-CHAIM model in Section 2; after which, a quiet-time model for NmF2 is presented in Section 3. A perturbation model to account for the general storm behaviour of NmF2, similar to the IRI's STORM model, is presented in Section 4 and a quiet-time hmF2 model is presented in Section 5. Each of these components is evaluated with respect to ionosonde observations that were not included in the fitting of the model and are compared to the performance of IRI-2007 at these locations.

2 The Empirical Canadian High Arctic Model (E-CHAIM)

E-CHAIM is intended as a replacement for the use of the IRI model at high latitudes. To this end, the model represents ionospheric electron density in the region above 50°N geomagnetic latitude. The model is composed of several sub-models, each representing a key feature in the ionospheric electron density profile. Like the IRI, NmF2 and hmF2 are chosen as the anchor point of the profile, with all other components representing characteristics with respect to the F2 peak density and height. Each of these sub-models feature a spherical cap harmonic expansion in the new Altitude-Adjusted Corrected Geomagnetic (AACGM) coordinates of Shepherd [2014], calculated at 350km altitude, for the representation of the horizontal structure of the modelled parameter. All further references to geomagnetic coordinates in this text refer to these 350km AACGM coordinates. These spherical cap harmonics are similar to those used in Weimer [1996], Liu et al. [2014], and Yamazaki et al. [2015]. The order and degree of this expansion is determined experimentally, based on the amount, distribution, and quality of available data. The seasonal variability is modelled by a Fourier expansion and solar cycle variability is modelled via a function of solar F10.7 cm flux and IG ionospheric index.

3 Quiet-time NmF2

The first phase of the E-CHAIM model is a climatological representation of NmF2, which will act as a reference point upon which to build the rest of the model.

3.1 Data

To represent the quiet-time behaviour of NmF2 at high latitudes, we have gathered ionogram data from 82 ionosondes. These ionosondes include data gathered from the Canadian High Arctic Ionospheric Network (CHAIN) available at http://chain.physics.unb.ca [Jayachandran et al., 2009], from the Global Ionospheric Radio Observatory (GIRO) available at http://giro.uml.edu/ [Reinisch and Galkin, 2011], from the now decommissioned Space Physics Interactive Data Resource (SPIDR), which was available at http://spidr.ionosonde.net/spidr, from the World Data Center for Solar-Terrestrial Physics (WDC for STP, Moscow) available at http://www.wdcb.ru/stp/index.en.html, from the United Kingdom Solar System Data Center (UKSSDC) available at http://www.ukssdc.ac.uk/, and from the EISCAT Scientific Association's Dynasonde Navigator available at http://dynserv.eiscat.uit.no/. The location of these ionosondes is presented in Figure 1. Stations included in the model fitting are marked with filled red circles, while stations used for validation are marked with X's. Note that some validation station locations coincide with the location of a station used in the model fitting. This is due to there being previous stations at those locations prior to the stations used for validation (ex: Resolute). For ionograms processed with the ARTIST autoscaling software (e.g. those from GIRO), only data with a quality control index of 70 or greater were included in the fitting dataset.

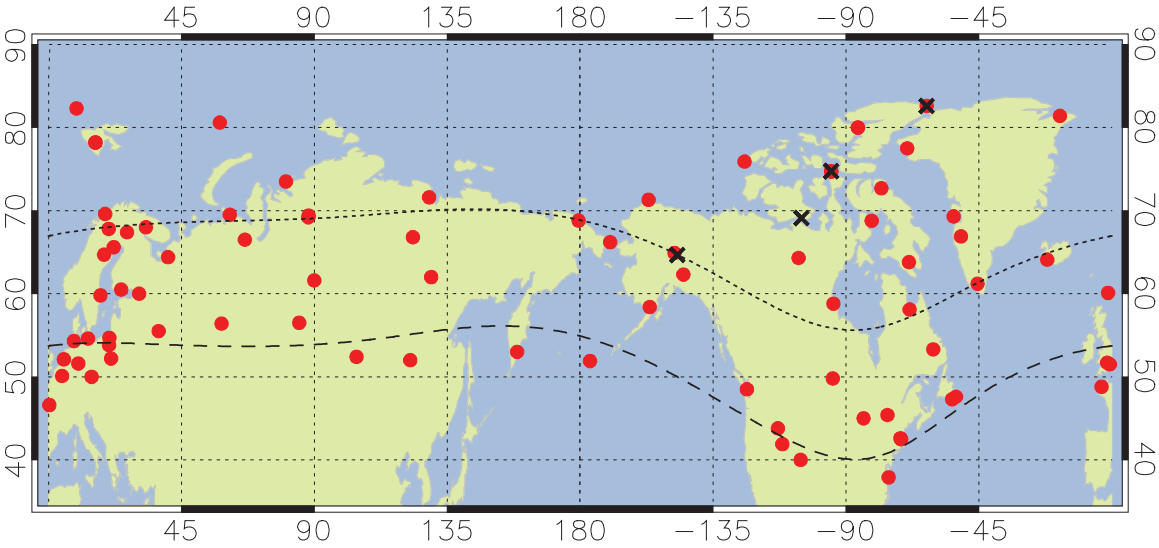

***Figure 1**. Plot of the global distribution of ionosondes used in the creation of the NmF2 phase of E-CHAIM. The dashed line corresponds to the lower boundary of the model at 50°N geomagnetic latitude. The dotted line corresponds to 65°N geomagnetic latitude.*

Radio Occultation (RO) data is also gathered from the CHAMP, Gravity Recovery and Climate Experiment (GRACE), and Constellation Observing System for Meteorology, Ionosphere, and Climate (COSMIC) missions, for all occultations above 45°N geomagnetic latitude. This data was gathered from the (CDAAC) data portal at http://cdaac-www.cosmic.ucar.edu/cdaac/. NmF2 and hmF2 were processed from these RO electron density profiles in a similar manner to that used in Shubin et al. [2013] and Shubin [2015].

For the purpose of the quiet-time model, only data corresponding to periods with Kp index less than 3.5 were included in the fitting dataset for this model. Overall, over 28 million data points are used in the fitting of the quiet-time NmF2 portion of the E-CHAIM model, spanning seven solar cycles between 1931 and 2016.

3.2 Model Parameterization

As mentioned in Section 2, the quiet-time NmF2 model is fitted by multiple linear regression (e.g. ordinary linear least squares) to a spherical cap harmonic function with Gauss coefficients tied to a Fourier expansion in day-of-year (DoY). The explicit parameterization of the model is as follows:

$$\log(NmF2) = G + \sum_{l=0}^{L} \sum_{m=0}^{\min(l,M)} \left[A_{lm} \cos\left(\frac{\pi m}{180}\lambda\right) + B_{lm} \sin\left(\frac{\pi m}{180}\lambda\right) \right] P_{lm}(\eta) \quad [1]$$

$$\eta = \cos\left((90 - \varphi)\frac{\pi}{45}\right) \quad [2]$$

$$A_{lm}, B_{lm} = (\gamma_{lm} F_1 + \delta_{lm} F_2) \cdot sin^2\left(\frac{\pi \cdot DoY}{365.25}\right) + (C_{lm} F_1 + D_{lm} F_2) \quad [3]$$

$$C_{lm}, D_{lm} = \sum_{c=1}^{K} \alpha_{lm}^{c} \cos\left(\frac{2\pi c \cdot DoY}{365.25}\right) + \beta_{lm}^{c} \sin\left(\frac{2\pi c \cdot DoY}{365.25}\right) \quad [4]$$

$$G = F10.7 \cdot (a_1 \cos(\chi) + a_2 \sin(\chi)) + \sqrt{F10.7} \cdot (a_3 \cos(\chi) + a_4 \sin(\chi)) + IG \cdot$$

$$(a_5 \cos(\chi) + a_6 \sin(\chi)) + a_7 F10.7^2 + a_8 IG^2 \quad [5]$$

$$F_1 = F10.7_{81} \qquad F_2 = (F10.7_{81})^{(1/1.9)} \quad [6]$$

where λ is magnetic local time, φ is geomagnetic latitude, DoY is the day of year, F10.781 is the 81-day smoothed F10.7 solar flux gathered from the NGDC portal at ftp://ftp.ngdc.noaa.gov/STP/GEOMAGNETIC_DATA/INDICES/KP_AP, IG is the monthly ionosonde-derived IG index gathered from the UKSSDC, and χ is the solar zenith angle. α, β, γ, δ, and a1-8 are fitting coefficients. The maximum degree (L) and order (M) for the spherical cap harmonic expansion were optimized via trial and error to be five and four, respectively. The Fourier expansion in DoY was chosen such that up to quintenial variations are represented (K = 5). This relatively high seasonal resolution was chosen such that short term (2-3 month) equinox enhancements, observed in polar cap NmF2, could be adequately represented by the model. This expansion results in 488 coefficients. Overall, these values were chosen to minimize the number

of artifacts in the NmF2 representation while providing a realistic representation of the spatial gradients present in the climatological high latitude ionosphere. This proved particularly challenging when trying to realistically represent the spatial extent of auroral region enhancements in NmF2 while avoiding the creation of artifacts in regions of little data, such as the Arctic Ocean region.

To represent diurnal variability, the model is actually composed of 24 separate models (e.g. 24 separate sets of Equations 1-6) fitted to data binned in UTC. To get the NmF2 at a given point in time, linear interpolation between the models is used. This approach is similar to that used in Shubin [2015] with their full spherical harmonic model. Attempts were made to use local time or geomagnetic local time as a longitudinal coordinate for a single model, such as that used in Altadill et al. [2009]; however, because of the coupled solar and geomagnetic control of NmF2 at these latitudes and the prevalence of UTC-dependant structures at high latitudes [Sojka et al., 1991], fits to such a single model were unsatisfactory.

Despite using 24 separate models, magnetic local time was selected as the longitudinal coordinate to partially account for within-hour variability. This geomagnetic latitude-magnetic local time coordinate system was chosen due to it providing a slight improvement in performance over similar pure-geographic, geographic latitude-local time, and pure-geomagnetic coordinate systems, which largely represented the differences in how well these systems could capture the within-hour variability of the dataset.

The functions of F10.7 flux and the additional group of G terms, used in the above model parameterization, were selected purely experimentally, via trial and error, and were chosen based on maximizing the fit correlation and minimizing the fit root mean square (RMS) error.

3.3 Model Validation

To validate the quiet-time portion of the E-CHAIM model, we have selected four validation datasets that were not included in the original fitting of the model; thus, we here test the predictive capability of the model and not just the model's ability to fit the dataset. The stations chosen are: Eielson, Alaska, (64.66°N, 212.91°E) a station that is generally near the equatorward boundary of the Auroral Oval; Cambridge Bay, Nunavut, (69.12°N, 254.88°E) a station that is generally at the poleward boundary of the Auroral Oval; Resolute, Nunavut, (74.75°N, 265.00°E) a Polar Cap Station; and Alert, Nunavut, (82.60°N, 297.40°E) another Polar Cap station but one closer to the region of data absence in the Arctic Ocean and to the geomagnetic and geographic poles. These four stations, represented as X's in Figure 1, provide reasonable coverage of the latitudinal domains expected to be represented by the model. It should be noted here that all data used for model validation in this study have been manually scaled to ensure the quality and accuracy of the validation datasets.

The validation of the quiet-time model primarily examines the model's capability to represent monthly median NmF2 and will include comparisons to the URSI foF2 maps of the IRI model. To that end, we present the monthly median NmF2 from all four validation sites in Figure 2. Please note that different time periods are examined by each validation station, purely as a result of data availability restrictions; nevertheless, these stations capture the solar minimum period of cycles 23-24, the solar maximum period of cycle 24, and the solar minimum period of cycles 22-23. Purely qualitatively, we see a significant improvement in the representation of NmF2 by the

E-CHAIM model. At all stations, we see a significant improvement in the representation of equinox, daytime NmF2, particularly at high solar activity. To a lesser extent, we see a significant improvement in the representation of NmF2 during the summer daytime at solar minimum. In addition to this, the use of 81-day smoothed F10.7 flux and monthly IG index allows the E-CHAIM model to partially represent the daytime NmF2 enhancements associated with short term increases in solar activity centered about December, 2011, and March, 2014, which are not captured by the IRI [Themens et al., 2016]. The magnitudes of the E-CHAIM-modeled enhancements are still, however, somewhat smaller than that observed by ionosonde, particularly at Cambridge Bay, leading the authors to suspect these enhancements are far more complex in origin than initially expected. Simulations with physics-based models will be necessary in order to properly assess the mechanism through which we observe these strong enhancements in ionospheric electron density.

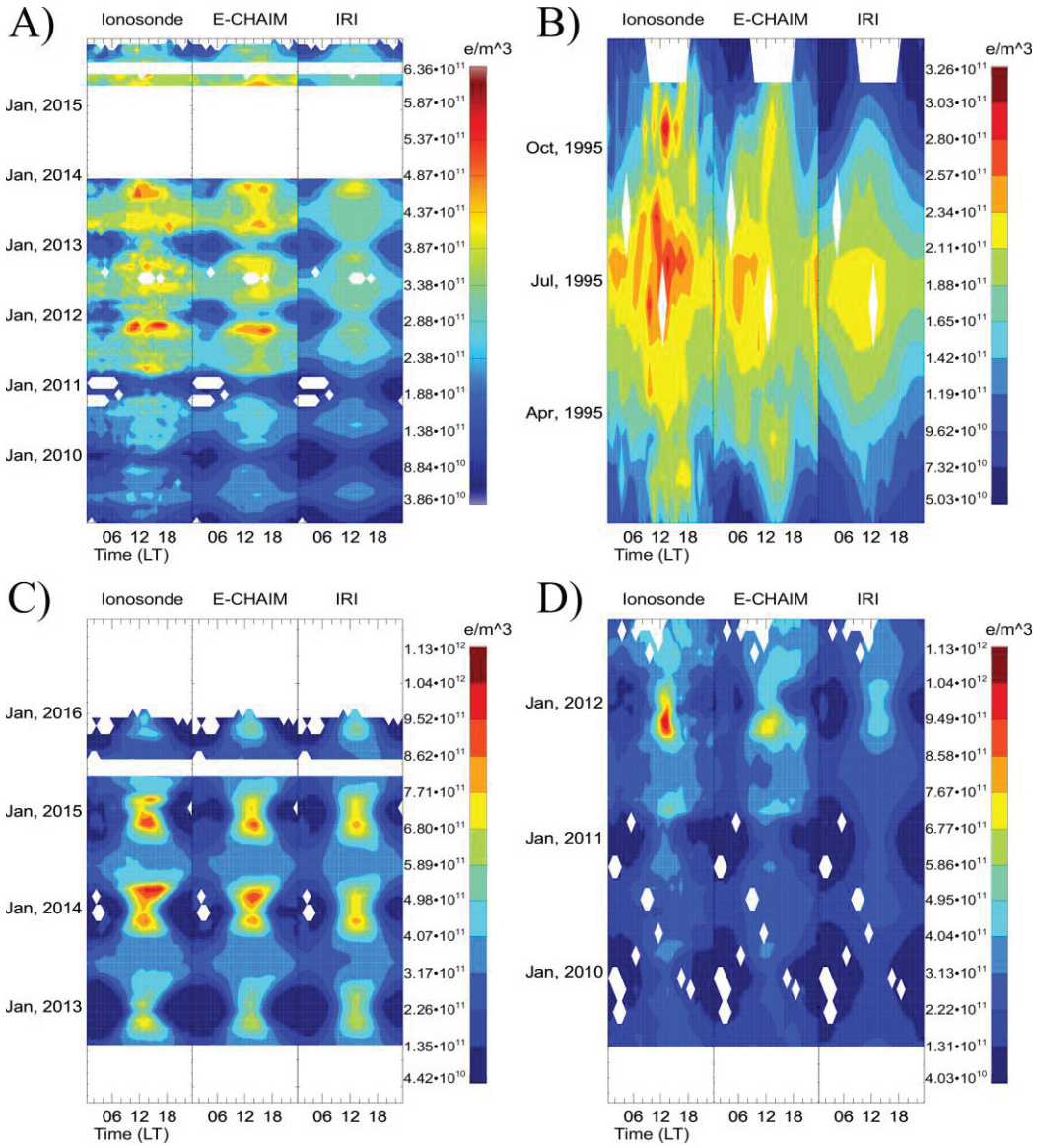

Figure 2. *Ionosonde-measured (left column), E-CHAIM-modeled (middle column), and IRI-modeled (right column) NmF2 for the Resolute (A), Alert (B), Eielson (C), and Cambridge Bay (D) validation stations.*

The apparent improvement, seen in Figure 2, is reinforced when comparing the RMS errors between the models in their representation of monthly median foF2, which are presented in Figure 3. foF2 was chosen for this comparison instead of NmF2 simply for its greater familiarity and simpler physical interpretation. Clearly from this figure we see a dramatic improvement in the representation of foF2 by the model at each of the polar cap stations, particularly at solar minimum and during the equinoxes, where improvements can be by as much as 1 MHz or more. At all stations, the E-CHAIM quiet-time model is either better than or matches IRI performance. These improvements diminish significantly as we progress to lower latitudes, which is somewhat

expected, as more data was available for the IRI fitting at those latitudes; that said, the improvements seen are still significant, particularly for low solar activity periods.

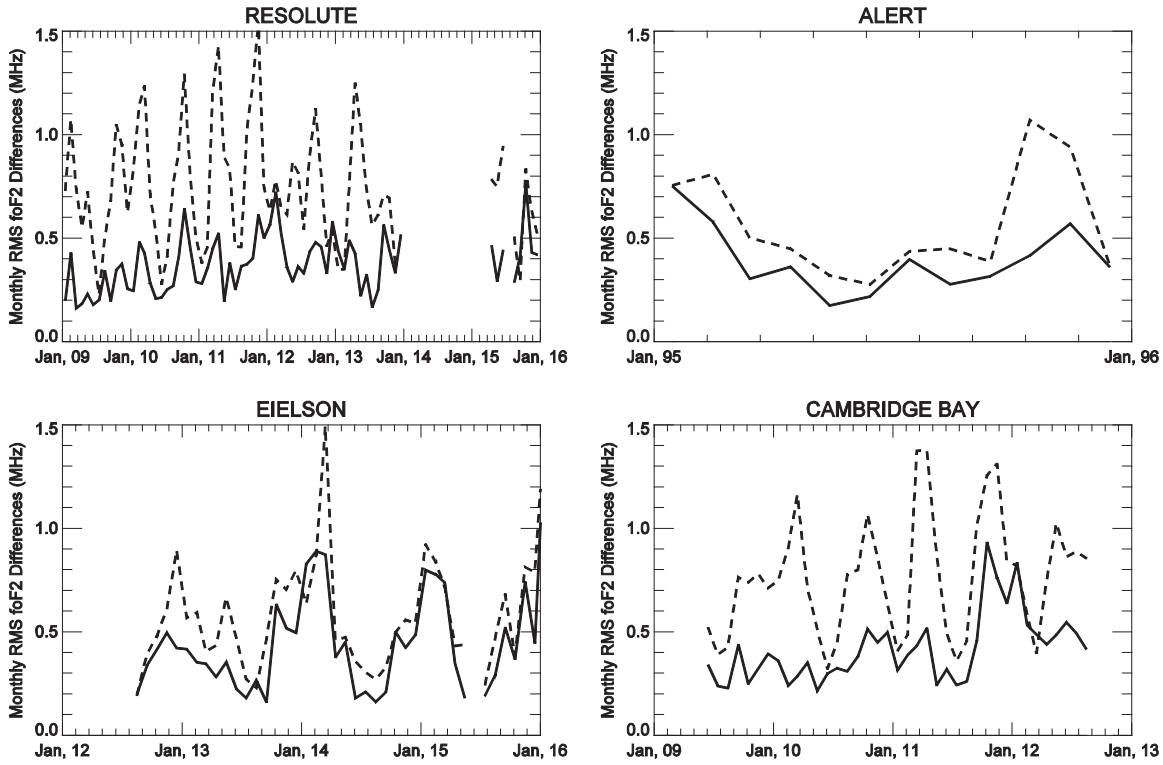

Figure 3. *Monthly RMS errors in E-CHAIM (solid line) and IRI (dashed line) foF2 at the Resolute (top left), Alert (top right), Cambridge Bay (bottom left), and Eielson (bottom right) validation stations.*

In terms of spatial variability, we present quiet-time foF2, generated by the E-CHAIM and IRI models, for 2013 in Figure 4. 2013 was chosen arbitrarily for illustration purposes. From this figure, we can easily distinguish the winter MIT and subsequent polar hole separated by an enhancement in foF2 in the auroral oval, not resolved by the IRI. During the summer we see a strong enhancement in foF2 extending from the dayside into the polar cap, which is also not represented in the IRI. Aside from structures we expect to see at high latitudes, such as the MIT and polar hole, one should note that without comparisons to datasets with large spatial coverage, truly assessing which model provides a more comprehensive representation of horizontal structures cannot be inferred from this Figure. In lieu of these types of observations, we must interpret this Figure in conjunction with previous studies of the IRI performance in these regions and with the comparisons provided previously in this study. From Figure 4, one sees that the E-CHAIM generally produces higher densities in the polar cap region with respect to those of the IRI with the exception of the nightside, where densities are lower. Given the IRI's cited tendency to underestimate foF2 in the polar cap during the equinox daytime and over estimate it during the equinox nighttime [e.g. Themens et al., 2014], this comes as no surprise. Also of interest is the E-CHAIM nighttime foF2 at 08 UTC, which is bisected by an enhancement extending from the dayside to the lower boundary of the model. In the IRI we see this bisection at all times of the day but only during and around winter periods. It is also interesting to note here that, had we used a

single model in local time or magnetic local time for the model's longitude coordinate in the spherical cap expansion, we would not see such differences between the E-CHAIM outputs at the various UTC times and would rather see the same structures simply rotated about the pole location.

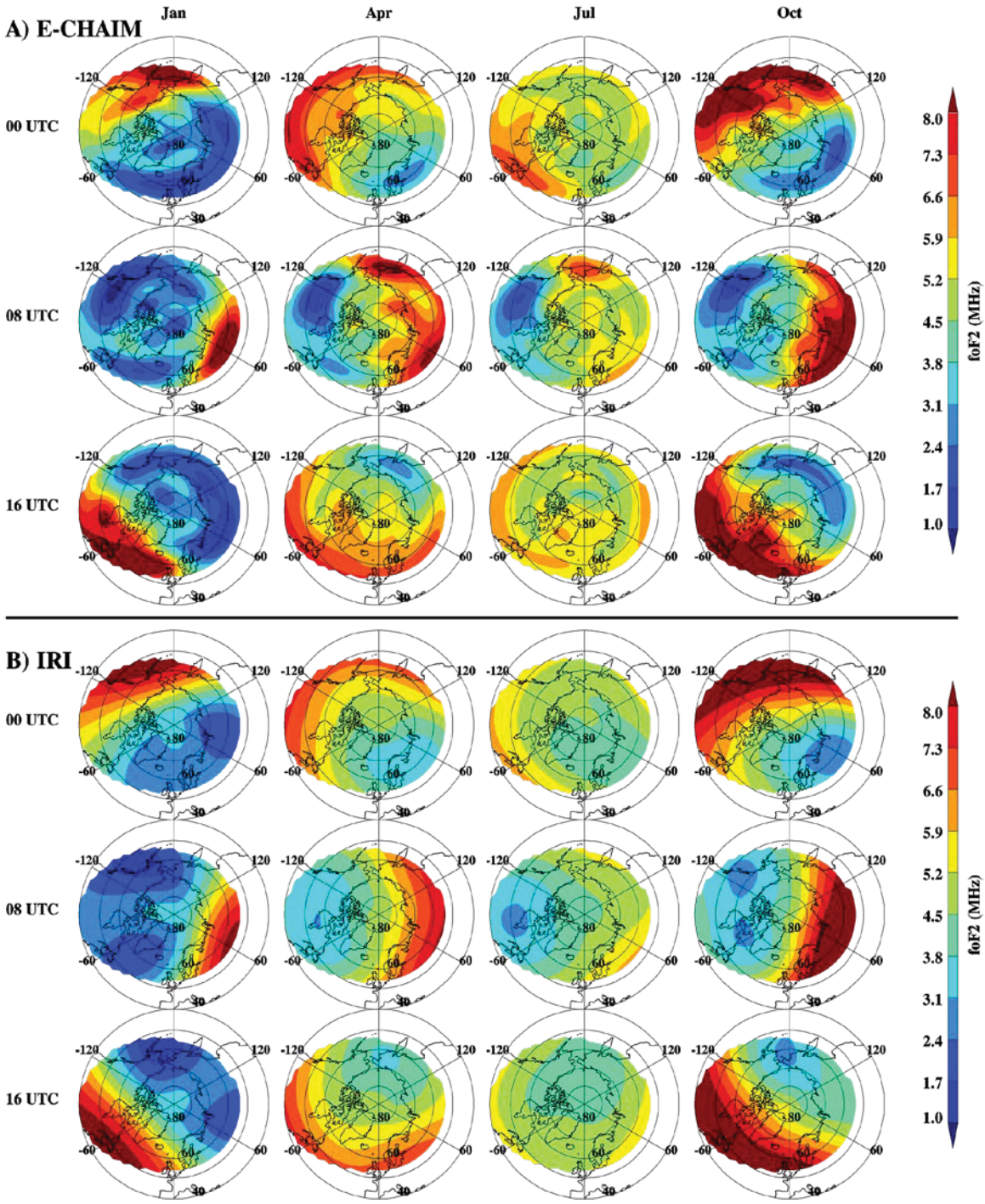

Figure 4. *Contours of foF2 from E-CHAIM (A) compared to that generated by the IRI (B), for representative months in 2013 at 00 (top row), 08 (middle row), and 16 (bottom row) UTC.*

Given the results of Themens et al. [2016], where the IRI demonstrated significant issues in representing TEC at high solar activity within the domain of this model, we feel it is important to also examine the seasonal and solar cycle variability of the E-CHAIM model. In Figure 5 we

present the slopes and correlations of fits between modelled and measured NmF2 at each local time hour at Resolute. In effect, these fits represent how well the models perform in their representation of seasonal and solar cycle variability at each of these times of day. If seasonal and solar cycle variability is well matched, we expect slopes of unity and strong, near unity, correlation coefficients. At Resolute, we see a consistent pattern of sub-unity slopes from both models, indicating a tendency to underestimate seasonal and solar cycle variability. Despite this, we see a significant improvement in both slope and correlation through the use of the E-CHAIM model over the IRI at nearly all local times. Resolute is taken as a representative location for consistency with previous studies: however, comparable features were seen at each of the other validation locations.

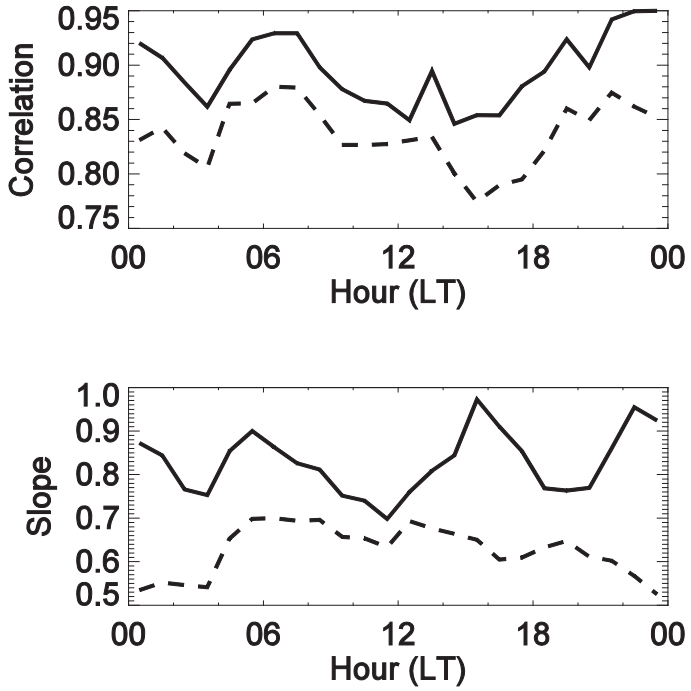

Figure 5. *Correlations (top) and slopes (bottom) for linear fits of IRI (dashed) and E-CHAIM (solid) NmF2 to that from the Resolute ionosonde for each local time hour.*

4 NmF2 Perturbation Model

In order to match the functionality of the IRI, we have also included an ionospheric storm correction to the quiet-time model. Empirical storm models, such as those of Araujo-Pradere and Fuller-Rowell [2002], Araujo-Pradere et al. [2002], and Li et al. [2016], are commonly used with simple geomagnetic indices to model the general ionospheric response to increased geomagnetic activity. While these models cannot be expected to represent all of the storm behaviour observed at high latitudes, given its highly dynamic nature and coupling to the solar wind, they can provide information on the overall large-scale ionospheric response.

4.1 Model Parameterization

The main driving parameters for this portion of the model were determined experimentally via trial and error and were selected as

$$\mathrm{G} = \left[e^{Dst\prime/300},\ e^{-ap\prime/30},\ e^{AE\prime/700}\right] \quad [7]$$

where G is a three-element array, Dst' is the integrated hourly Dst index from the Kyoto World Data Center (WDC) for Geomagnetism (available at http://wdc.kugi.kyoto-u.ac.jp/), ap' is the integrated three-hour ap index from the NGDC portal, and AE' is the integrated hourly AE index gathered from the Kyoto WDC for Geomagnetism. The geomagnetic activity indices, used here, are integrated forms of the Dst, Ap, and AE indices, where integration is done in the same manner as Wu and Wilkinson [1995] with persistence factors of 0.95, 0.75, and 0.95, respectively. Persistence factors were determined purely by trial and error using the values provided in Perrone et al. [2001] and Wu and Wilkinson [1995] as starting points. The functions, G, of the above geomagnetic indices were arrived at purely through extensive trial and error.

Using a spherical cap harmonic expansion to represent horizontal variability in ionospheric storm response and the sine and cosine of the dipole tilt angle as a seasonal term, we have the following for the storm model parameterization

$$\log\left(\frac{NmF2}{\overline{NmF2}}\right) = \sum_{l=0}^{L}\sum_{m=0}^{\min(l,M)}\left[A_{lm}\cos\left(\frac{\pi m}{180}\lambda\right) + B_{lm}\sin\left(\frac{\pi m}{180}\lambda\right)\right]P_{lm}(\eta) \quad [8]$$

$$A_{lm}, B_{lm} = \sum_{d=1}^{3}\left[\alpha_{lm}\sin\theta + \beta_{lm}\cos\theta + (\gamma_{lm}\sin\theta + \delta_{lm}\cos\theta)\sqrt{F10.7_{81}}\right]G_d \quad [9]$$

where λ is magnetic local time, φ is geomagnetic latitude, F10.781 is the 81-day smoothed F10.7 solar flux, and θ is the magnetic dipole tilt angle. α, β, γ, and δ are fitting coefficients. Gd refers to the dth element of the G array, given by Equation 7. The maximum order and degree of the expansion was set to five and three, respectively, for this portion of the model. The reduced degree of the spherical cap expansion is a consequence of the reduction in the quality of

ionosonde data during geomagnetic storm events, which tended to exaggerate noise in the storm output. There are 360 coefficients for each of the 24 hourly UTC models.

4.2 Performance and Examples

To demonstrate the performance of the storm/perturbation model, we have scaled ionograms from the Resolute, Cambridge Bay, Pond Inlet (72.69N, 262.04E), and Eureka (79.99N, 274.10E) stations. For these stations, we compare measured and modeled NmF2 for a moderate, and fairly long-lived, storm between May 21 and June 7, 2010, in Figure 6.

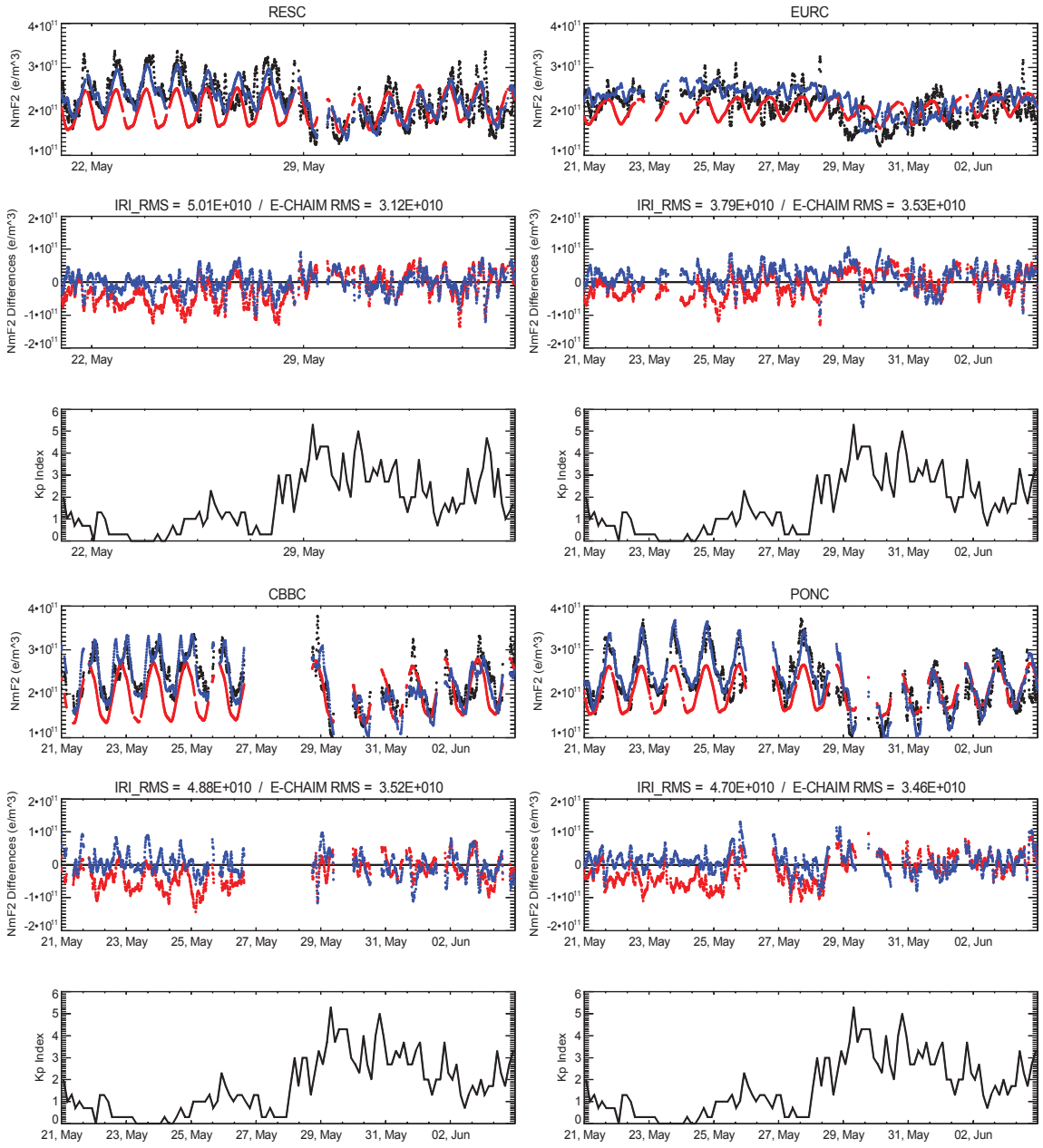

Figure 6. *(top row of each quadrant) Ionosonde-measured (black), E-CHAIM modeled (blue), and IRI-modeled (red) NmF2 around the May 29th, 2010 geomagnetic storm at the Resolute (top left - RESC), Eureka (top right - EURC), Cambridge Bay (bottom left - CBBC), and Pond Inlet (bottom right - PONC) validation stations. (middle row of each quadrant) Differences between observations and the E-CHAIM (blue) and IRI (red) modeled observations for the corresponding stations. (bottom row of each quadrant) Kp index for the periods presented.*

It is clear from Figure 6 that the E-CHAIM perturbation model performs well in representing NmF2 during this storm at all four stations, with the exception of Eureka at storm onset, where we see a delay in the modeled storm response from both E-CHAIM and the IRI. We clearly see a

strong negative phase response in observed NmF2 that is captured by both the E-CHAIM perturbation model and the IRI. Interestingly, the IRI also performs reasonably well during this storm, despite significant issues during the quiet periods preceding and following the storm; in fact, the IRI performs better during the storm period than during quiet periods. This, however, implies that the IRI is underestimating the storm response of the ionosphere with respect to quiet periods (e.g. the difference between storm and climatological NmF2). In terms of improvement over the climatological E-CHAIM model, the perturbation model results in a 33% improvement at Resolute, a 22% improvement at Eureka, an 18% improvement at Cambridge Bay, and a 30% improvement at Pond Inlet.

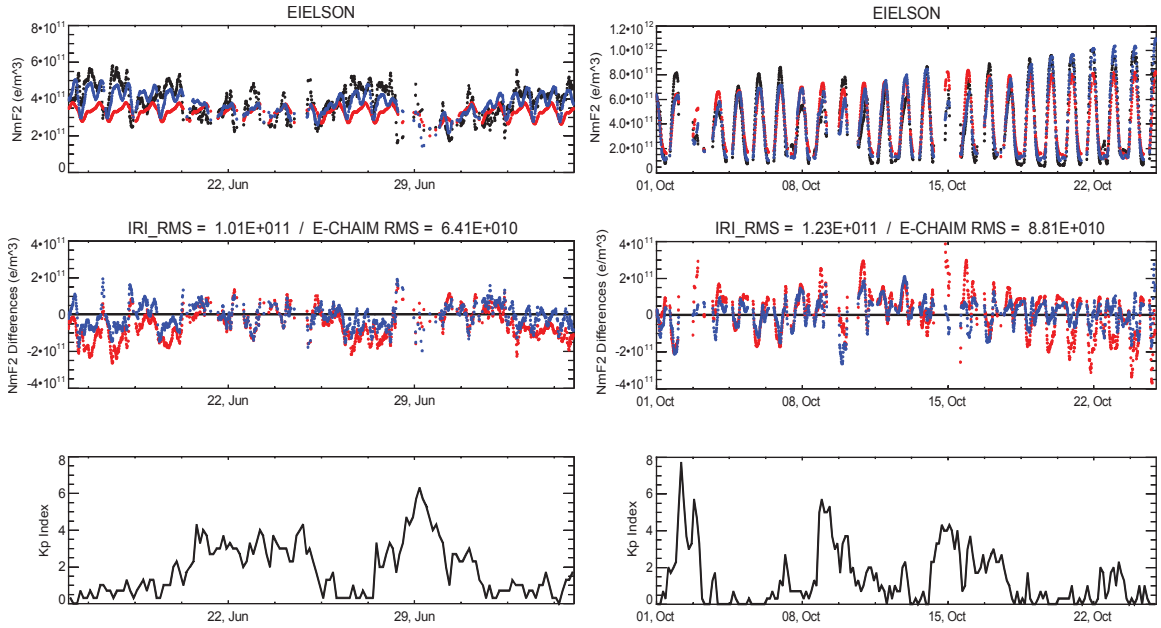

Figure 7. *Same as Figure 6 but for Eielson between June 15th and July 5th, 2013 (left) and October 1st and October 25th, 2013 (right).*

For the auroral region, we also present NmF2 at Eielson for a pair of disturbed periods in June and October, 2013, in Figure 7. For the June period, we again see a tendency for the IRI to underestimate quite-time NmF2 and see much better performance from the E-CHAIM model. Total RMS errors during these periods (listed in the figure headers) show a 30-35% improvement over the IRI through the use of E-CHAIM, mostly coming from quiet-time improvements. During storm periods, however, both models converge to similar density representations. For the October period, we see much of the same. There are, however, a few interesting features in the October period:

1) a relatively weak increase in geomagnetic activity on October 7th appears to generate a strong ionospheric response that is not captured by either model;

2) E-CHAIM shows slightly better performance during the Kp 7+ geomagnetic storm on October 2nd, where E-CHAIM matches the main phase and early recovery phase to within 0.5e11 while the IRI overestimates by up to 3e11. During the remainder of the storm recovery phase, E-CHAIM shows only minor improvements over the IRI of about

0.5e11 before becoming virtually identical to the IRI during the post recovery quiet period;

3) neither model captures the enhanced (above climatological) daytime density proceeding the recovery from the October 2nd storm; and

4) E-CHAIM correctly captures the quiet-time density following the last storm of the period.

Features 1 and 3, to some extent, highlight the limitations of empirical storm models in their application at high latitudes; nonetheless, these first order adjustments constitute a significant improvement over the climatological density. For the periods at Eielson, the perturbation model resulted in 24% improvements over the climatological E-CHAIM model. Further improvements to storm NmF2 representations, to account for features like patches, will likely need to come in the form of data assimilation, perhaps using an empirical background model, such as E-CHAIM.

5 Quiet-time hmF2

The electron density of the complete E-CHAIM model will be parameterized with respect to both the peak density and height of the ionosphere, which necessitates the development of an accurate hmF2 model.

5.1 Data

The bulk of the ionosonde data included in the following model is derived from POLAN- or ARTIST-inverted ionograms [Titheridge, 1988; Huang and Reinisch, 2001]. Due to the additional difficulty in processing hmF2 from ionograms, particularly at high latitudes, additional quality control measures were necessary in order to ensure outliers and poorly processed data were removed [Moskaleva and Zaalov, 2013]. To this end, in addition to the quality control measures applied to the foF2 data, when original ionograms were available, suspect auto-scaled data were verified visually by an experienced ionogram scaler and corrected, if necessary.

In addition to directly inverted ionosonde hmF2 data and GPS RO data, we have also included hmF2 data inferred via the Bradley-Dudeney method, as provided by the SPIDR system [Bilitza et al., 1979]. This data was found to be consistent with that derived from ionogram inversion and was thus included in the model fitting.

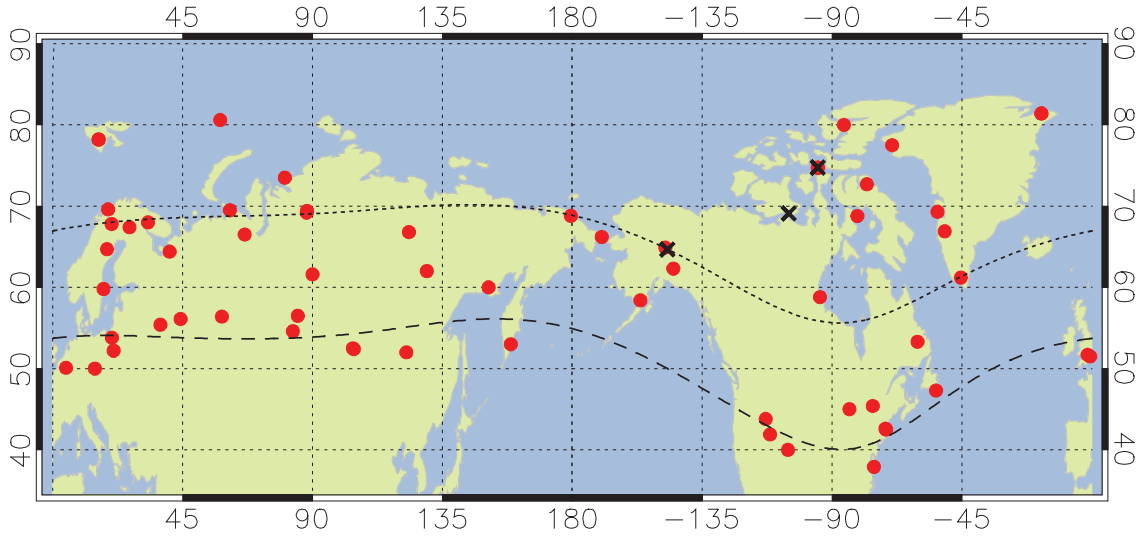

Figure 8. *Plot of the global distribution of ionosondes used in the creation of the hmF2 phase of E-CHAIM. The dashed line corresponds to the lower boundary of the model at 50°N geomagnetic latitude. The dotted line corresponds to 65°N geomagnetic latitude.*

A map of the ionosonde stations used for the hmF2 portion of the model is presented in Figure 8, where red filled circles mark the locations of stations included in the fitting and X's mark the locations of stations used in the validation of the model. Note that some validation station locations coincide with the location of a station used in the model fitting. This is due to there being previous stations at those locations prior to the stations used for validation (ex: Resolute). Overall, ~15 million data points are used in the fitting of the hmF2 model, spanning seven solar

cycles. Similar to the quiet-time NmF2 model, only data corresponding to Kp values less than 3.5 are included in the fitting dataset for the quiet-time hmF2 model.

5.2 Model Parameterization

The hmF2 model features a similar parameterization to that for climatological NmF2 with some adjustments to take into account different solar activity scaling, a greater solar zenith angle and dipole tilt dependence, and a significant reduction in the amount of high quality data available for model fitting. The explicit parameterization is given as:

$$hmF2 = G + \sum_{l=0}^{L} \sum_{m=0}^{\min(l,M)} \left[A_{lm} \cos\left(\frac{\pi m}{180}\lambda\right) + B_{lm} \sin\left(\frac{\pi m}{180}\lambda\right) \right] P_{lm}(\eta) \quad [10]$$

$$\eta = \cos\left((90 - \varphi)\frac{\pi}{45}\right) \quad [11]$$

$$A_{lm}, B_{lm} = (\gamma_{lm} F_1) \cdot sin^2\left(\frac{\pi \cdot DoY}{365.25}\right) + (C_{lm} F_1) \quad [12]$$

$$C_{lm}, D_{lm} = \sum_{c=1}^{K} \alpha_{lm}^{c} \cos\left(\frac{2\pi c \cdot DoY}{365.25}\right) + \beta_{lm}^{c} \sin\left(\frac{2\pi c \cdot DoY}{365.25}\right) \quad [13]$$

$$G = F10.7 \cdot (a_1 \cos(\chi) + a_2 \sin(\chi)) + \sqrt{F10.7} \cdot (a_3 \cos(\chi) + a_4 \sin(\chi)) + IG \cdot$$

$$(a_5 \cos(\chi) + a_6 \sin(\chi)) + a_7 F10.7^2 \cos(\chi) + a_8 IG^2 + cos(\chi) \cdot [a_9 sin(\theta) +$$

$$a_{10} cos(\theta)] + sin(\chi) \cdot [(a_{11} sin(\theta) + a_{12} cos(\theta))] \quad [14]$$

$$F_1 = F10.7_{81}^{0.275} \quad [15]$$

where α, β, γ, and a1-12 are fitting coefficients. The solar activity scaling term F1 was chosen based on trial and error by iterating through powers of F10.781 between 0.1 and 4.0 in steps of 0.025. Due to the increased noise, decreased reliability, and poor distribution of hmF2 data, particularly, at high latitudes, the hmF2 model features a drastically reduced spatial order and degree of three and three (L = 3, M = 3), respectively, but the same, quintenial, seasonal Fourier Expansion (K = 5) as the NmF2 model. This model has 122 coefficients for each of the 24 UTC hourly models. Despite the drastically reduced spherical cap expansion, the model still demonstrates significantly more spatial structuring than the IRI2007 hmF2 model, which can be seen in Figure 9, where we present maps of the E-CHAIM- and IRI2007-modeled hmF2 for 2013, similar to Figure 4.

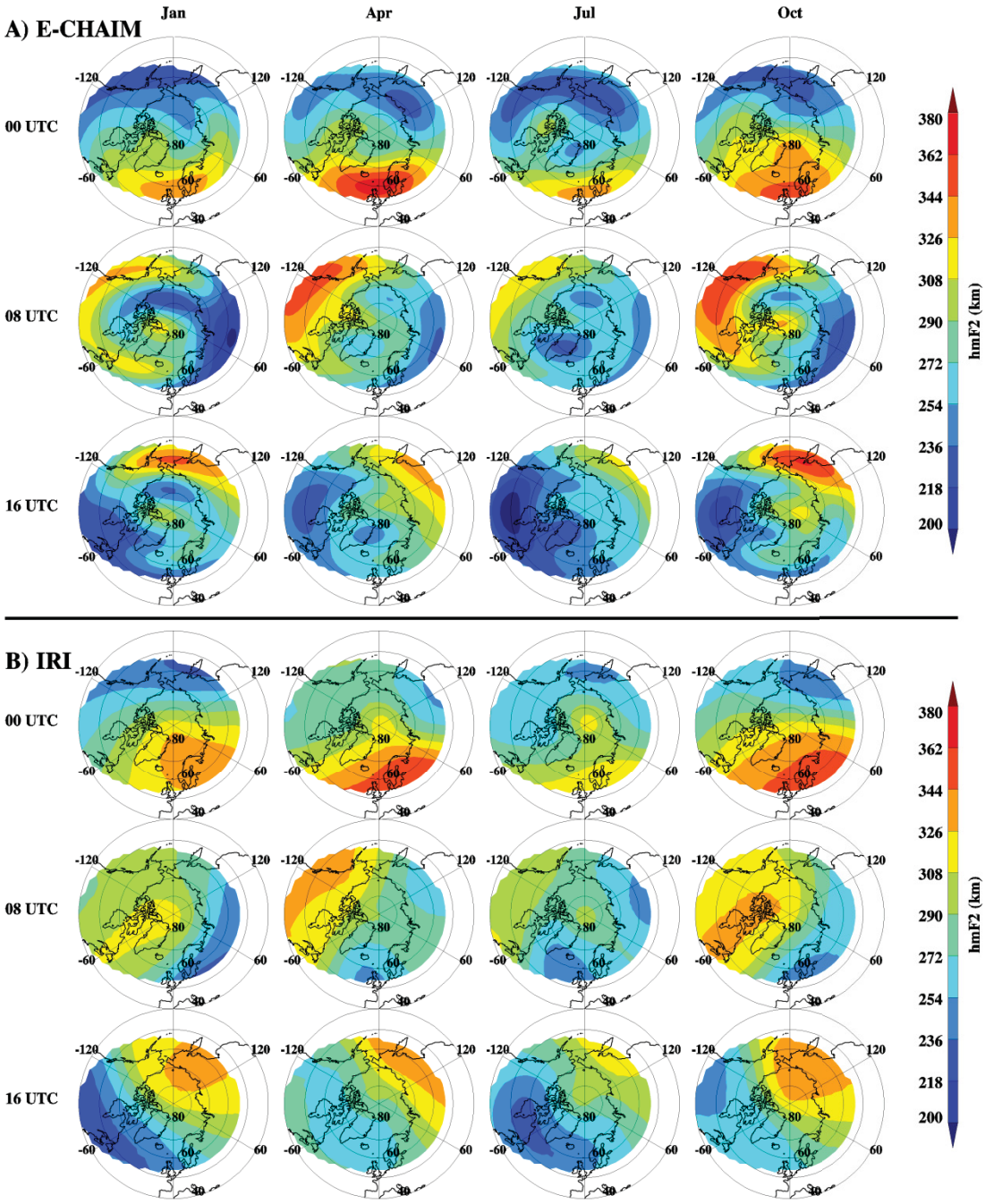

Figure 9. *Contours of hmF2 from E-CHAIM (A) compared to that generated by the IRI (B), for representative months in 2013 at 00 (top row), 08 (middle row), and 16 (bottom row) UTC.*

In Figure 9, there is drastically more structuring in the E-CHAIM representation than in the IRI maps, despite the relatively low order and degree of the spherical cap expansion. Please note that IRI2007 was used here as it features an identical hmF2 parameterization as IRI2012. While IRI2016 features the Shubin [2015] and Altadill et al. [2013] hmF2 models, at the time this work was completed, IRI2016 had only just been released. Regardless of this, the authors felt that, for

consistency with previous studies [Themens et al., 2014], the use of the pre-2016 model was sufficient here. Future studies will examine comparisons between the new IRI2016 hmF2 parameterizations and that of the E-CHAIM model.

There are several interesting differences between the E-CHAIM and IRI spatial patterns in modeled hmF2. The IRI demonstrates a local maximum in hmF2 over the geographic pole during summer periods, not seen in the E-CHAIM results. The E-CHAIM shows an enhancement of this sort; however, its enhancement is located closer to the geomagnetic pole and occurs primarily during winter and equinox periods. E-CHAIM also shows a deep minimum/trough in hmF2 in the auroral region, particularly during the winter, while the IRI demonstrates no such feature. In general, E-CHAIM produces lower dayside hmF2 compared to the IRI and higher nightside hmF2. Also, at 08 UTC during spring and summer periods, the IRI shows an enhancement in hmF2 at local noon that stretches from the pole to mid latitudes. In E-CHAIM, a comparable enhancement is seen; however, this enhancement only extends to the auroral region, with a subsequent hmF2 minimum/trough at lower latitudes.

5.3 Model Validation

To validate the hmF2 portion of the model, we use hmF2 values derived from ionosondes at Resolute, Cambridge Bay, and Eielson. Comparisons between observed, E-CHAIM, and IRI hmF2 are presented in Figure 10. Immediately evident here is a drastic improvement over the IRI in the hmF2 representation at Eielson by E-CHAIM during daytime periods, where the IRI appears to consistently overestimate hmF2. This improvement is likely associated with E-CHAIM's representation of an auroral hmF2 trough, demonstrated in Figure 9, which is represented in the IRI at lower latitudes and as a much broader structure. During the nighttime at Eielson, we see a slight improvement through using E-CHAIM; however, both models are reasonably comparable during these periods. At Cambridge Bay and Resolute, we see a much deeper seasonal nighttime minimum in the winter. Also, observations show a daytime hmF2 maximum during the winter at low solar activity transitioning into a maximum in each equinox at higher solar activity. The IRI shows this single maximum in the winter at low solar activity but does not make the transition into maxima in each equinox. E-CHAIM shows much stronger performance in representing these features, particularly at Resolute.

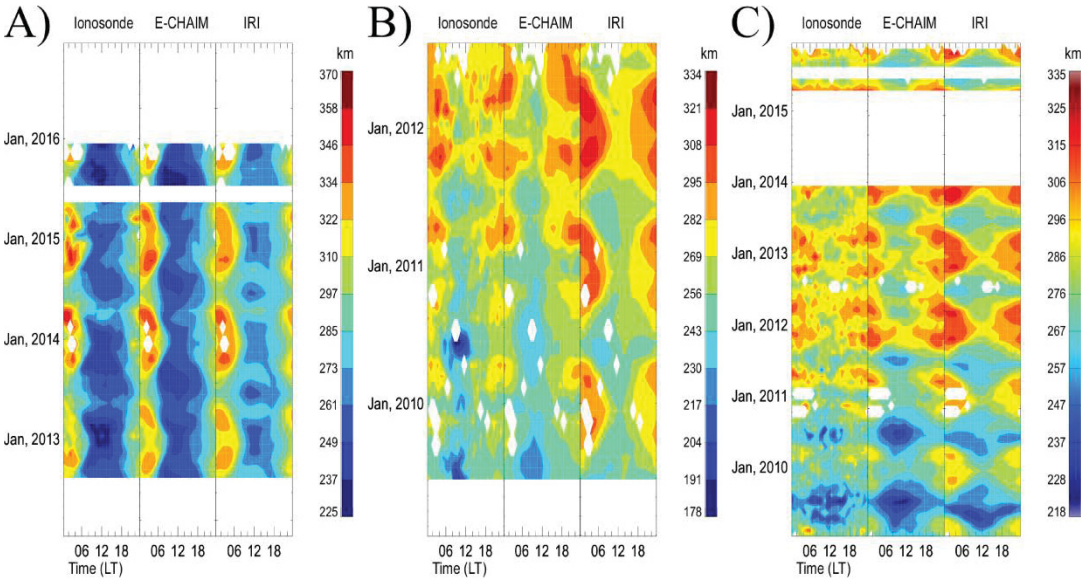

Figure 10. *Ionosonde-measured (left column), E-CHAIM-modeled (middle column), and IRI-modeled (right column) hmF2 for the Eielson (A), Cambridge Bay (B), and Resolute (C) validation stations.*

Over the periods presented in Figure 10, the overall RMS errors for hmF2 produced by E-CHAIM are roughly the same for all three sites at between 13.0km and 13.5km; however, the IRI demonstrates RMS errors of 15.7 km at Resolute, 18.5 km at Cambridge Bay, and 22.2 km at Eielson. The seasonal patterns in these RMS errors are presented in Figure 11. At Resolute, we see only a marginal improvement in hmF2, mostly concentrated in winter and summer periods, and is otherwise largely comparable to the IRI. At Cambridge Bay, we see much more significant improvements, particularly during winter periods, where errors are reduced by as much as 20 km. At Eielson, we again see significant improvement over the IRI by as much as 20 km, this time during equinox periods, which are largely associated with the IRI's overrepresentation of daytime, equinox maxima. Overall, both models perform reasonably well at the test locations; however, the E-CHAIM shows significant improvements over the IRI2007 representation in the auroral oval region.

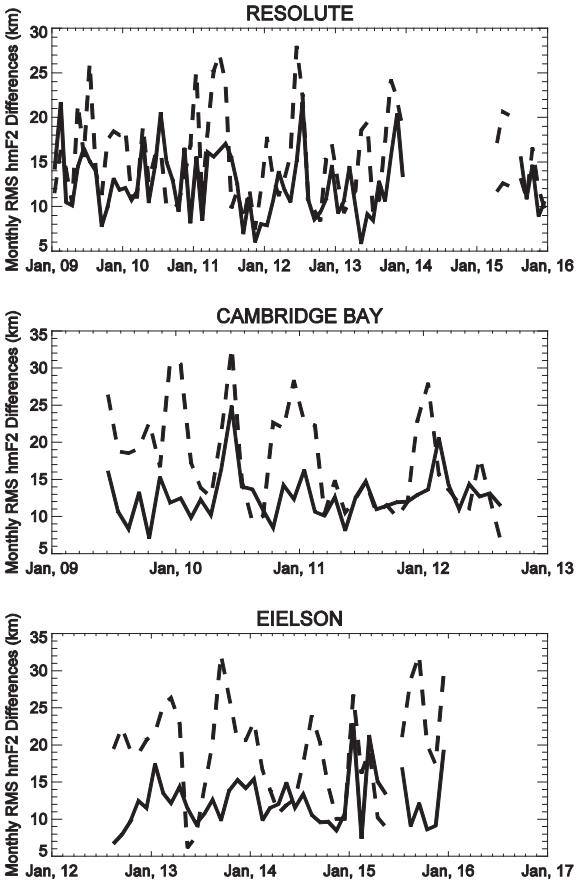

Figure 11. *Monthly RMS errors in E-CHAIM (solid line) and IRI (dashed line) hmF2 at the Resolute (top), Cambridge Bay (middle), and Eielson (bottom) validation stations.*

5.4 Future Development

Incorporation of the E-CHAIM specification of the high-latitude ionosphere in the IRI, so as to produce an improved standard of the global ionospheric density distribution would be highly desirable; however, differences between the IRI and E-CHAIM are unbridgeable at the model junctions along E-CHAIM's lower boundary. Use of such a hybrid model in scenarios that require density definitions across the models' boundary (e.g. for ray tracing applications) would then be prohibitive. Retraining the IRI expansions of foF2 and hmF2 in the E-CHAIM formalism can be considered, but this would require fundamental refitting of the entire IRI model, due to the internal dependence on foF2 maps, which may be prohibitive. .

There is, however, an attractive option of incorporating E-CHAIM maps of NmF2 and hmF2 in the IRI-based Real-Time Assimilative Model (IRTAM) [Galkin et al., 2012], whichperiodically generates updated IRI coefficients to transform the IRI into a better match with available measurements provided by contributing ionosondes of the Global Ionosphere Radio Observatory (GIRO) [Reinisch and Galkin, 2011]. By design, IRTAM gradually returns to the background IRI in those regions where sensor data are not available for assimilation. The E-CHAIM synthesized data grids can override the IRI background at high latitudes during IRTAM's spatial expansion

stage of analysis. IRTAM will then protect such a combined grid from discontinuity artifacts across junctions in the same way it operates with GIRO data, by applying its iterative 2D smoothing neural network algorithm and expanding the grid into the Jones-Gallet Gk basis [ITU-R, 2009]. The resulting IRTAM will thus include all sensor data, the improved E-CHAIM high latitude model, and the background IRI over no-coverage areas in a single global specification that is continuous in time and space.

Including the E-CHAIM model in the IRTAM, as well as other assimilation frameworks, will be pursued in future work.

6 Conclusion

The work presented herein details the model description and validation for the E-CHAIM quiet NmF2, perturbation NmF2, and quiet hmF2 models. All three models consist of a spherical cap harmonic expansion for the representation of horizontal variations, F10.7 flux parameterizations for variations associated with solar activity, and separation into 24 separate UTC maps to account for diurnal variations. The quiet models both also feature Fourier expansions in day of year, with up to quintenial terms, to represent seasonal variations and additional terms in solar zenith angle, IG index, and dipole tilt angle to improve performance.

In the case of the quiet NmF2 model, the E-CHAIM model provides a systematic improvement over the IRI URSI maps in terms of RMS errors. At all stations within the polar cap, we see drastic improvements over the IRI by up to 1.3MHz in critical frequency (up to 60% in NmF2), primarily during equinox periods and at low solar activities. At the lower boundary of the auroral oval, we see less drastic contrasts in performance, where E-CHAIM represents a significant improvement over the IRI only outside of solar maximum and during periods characterized by short term solar activity enhancements. Qualitatively, the E-CHAIM model features a significant improvement in horizontal resolution over the IRI, where E-CHAIM is capable of representing auroral enhancements in NmF2, as well as the location and extent of the MIT, which the IRI could not resolve.

To match the functionality of the IRI, the E-CHAIM model also features a storm-time adjustment model to account for ionospheric variations associated with storm periods. Comparing this storm model to that of the IRI during a prolonged Kp = 5 storm beginning on May 29, 2010, we see a significant improvement over the IRI's representation of the ionospheric response to increased geomagnetic activity. During this period, the storm parameterization constitutes an 18%-33% improvement over the climatological model. Similarly, during two test periods at Eielson (June 15 - July 5 and October 1 – 25, 2013), we see an average improvement by 30% – 35% over the IRI performance and a ~24% improvement over the quiet-time E-CHAIM model performance. At Eielson, in particular, the majority of these improvements came from the quiet periods between storms. During the storms themselves, E-CHAIM showed a slight improvement over the IRI, but ultimately, both models tended to converge to one another. In all cases, to our surprise, the IRI performed better during storm periods than during quiet periods.

In terms of hmF2, the E-CHAIM model performance was generally within 20km. Over the validation periods used in this study, we found overall RMS errors of ~13km for E-CHAIM, with IRI2007 overall hmF2 errors ranging between 16km and 22km. Within the polar cap, both models perform reasonably well; however, as one tends toward lower latitudes, the E-CHAIM model generally constitutes a universal improvement over the IRI2007 model, where improvements largely came during winter and equinox periods. Future studies will undertake a comparison between the E-CHAIM and Shubin [2015] hmF2 model employed by the recently released IRI2016.

Despite the strong performance of these models at the validation stations, there remain potentially unexplored limitations of the model, particularly in regions where data is lacking, such as the Arctic Ocean and the North Atlantic Ocean regions. More extensive validations of the model in these regions with alternative instruments are invited.

Once a model distribution package has been completed, an online visualization tool and C code will be made available at http://chain.physics.unb.ca.

References/Bibliography

Altadill, D., J.M. Torta, and E. Blanch (2009), Proposal of new models of the bottom-side B0 and B1 parameters for IRI. *Adv. Space Res.*, 43, 1825-1834, doi:10.1016/j.asr.2008.08.014

Altadill, D., S. Magdaleno, J.M. Torta, and E. Blanch (2013), Global empirical models of the density peak height and of the equivalent scale height for quiet conditions, *Adv. Space Res.*, 52, 1756-1769, doi:10.1016/j.asr.2012.11.018

Athieno, R., P. T. Jayachandran, D. R. Themens, and D. W. Danskin (2015), Comparison of observed and predicted MUF(3000)F2 in the polar cap region. *Radio Sci.*, 50, 509–517, doi:10.1002/2015RS005725.

Athieno, R., and P.T. Jayachandran (2016), MUF variability in the Arctic region: A statistical comparison with the ITU-R variability factors. Radio Sci., 51, 1278–1285, doi:10.1002/2016RS006096.

Araujo-Pradere, E.A., T. J. Fuller-Rowell, and M. V. Codrescu(2002), STORM: An empirical storm-time ionospheric correction model, 1, Model description, Radio Sci., 37(5), 1070,doi:10.1029/2001RS002467.

Araujo-Pradere, E. A., and T. J. Fuller-Rowell (2002), STORM: An empirical storm-time ionospheric correctionmodel, 2, Validation, Radio Sci., 37(5), 1071, doi:10.1029/2002RS002620.

Bilitza, D., N. M. Sheikh, and R. Eyfrig (1979), A global model for the height of the F2-peak using M3000 values from the CCIR numerical map, Telecommun. J., 46, 549–553.

Bilitza, D., and B. W. Reinisch (2008), International Reference Ionosphere 2007: Improvements and new parameters, Adv. Space Res., 42, 599–609, doi:10.1016/j.asr.2007.07.048.

Bilitza, D., et al. (2017), International Reference Ionosphere 2016: from ionospheric climate to real-time weather predictions. J. Geophys. Res. Space Physics, 15(2), 418 – 429, doi:10.1002/2016SW001593

Bjoland, L.M., V. Belyey, U.P. Lovhaug, and C. La Hoz (2016), An evaluation of International Reference Ionosphere electron density in the polar cap and cusp using EISCAT Svalbard radar measurements. Ann. Geophys., 34, 751-758, doi:10.5194/angeo-34-751-2016

Cacciamano A, Capria A, Berizzi F, et al. (2009). Proceedings of the 6th European Radar Conference, 204 -207.

Coïsson, P., S.M. Radicella, R. Leitinger, and B. Nava (2006), Topside electron density in IRI and NeQuick: Features and limitations, Advances in Space Research, 37(5), 937-942, doi:10.1016/j.asr.2005.09.015

Galkin, I. A., B. W. Reinisch, X. Huang, and D. Bilitza (2012), Assimilation of GIRO Data into a Real-Time IRI, *Radio Sci.,* 47, RS0L07, doi:10.1029/2011RS004952.

Hoque, M.M., and N. Jakowski (2011), A new global empirical NmF2 model for operational use in radio systems. Radio Sci., 46, RS6015, doi:10.1029/2011RS004807

Hoque, M.M., and N. Jakowski (2012), A new global model for the ionospheric F2 peak height for radio wave propagation. Ann. Geophys., 30, 797–809, doi:10.5194/angeo-30-797-2012

Huang, X., and B. W. Reinisch (2001), Vertical electron content from ionograms in real time, *Radio Sci.*, 36, 335-342.

International Telecommunications Union (2009), *ITU-R reference ionospheric characteristics, Recommendation P.1239-2* (10/2009). Retrieved from http://www.itu.int/rec/R-REC-P.1239/en on May 22, 2017.

Jayachandran, P. T., R. B. Langley, J. W. MacDougall, S. C. Mushini, D. Pokhotelov, A. M. Hamza, I. R. Mann, D. K. Milling, Z. C. Kale, R. Chadwick, T. Kelly, D. W. Danskin, and C. S. Carranoet (2009), Canadian High Arctic Ionospheric Network (CHAIN), Radio Sci., 44, RS0A03, doi: 10.1029/2008RS004046.

Karpachev, A.T., M.V. Klimenko, V.V.Klimenko, and L.V. Pustovalova (2016), Empirical model of the main ionospheric trough for nighttime winter conditions. J. Atm. Sol.-Ter. Phys., 146, doi:10.1016/j.jastp.2016.05.008

Li, S., R. Galas, D. Ewert, and J. Peng (2016), An empirical model for the ionospheric global electron content storm-time response. Acta Geophysica, 64(1), 253-269, doi:10.1515/acgeo-2015-0067

Liu, J., R. Chen, J. An, Z. Wang, and J. Hyyppa, (2014), Spherical cap harmonic analysis of the Arctic ionospheric TEC for one solar cycle, J. Geophys. Res. Space Physics, 119, 601-619, doi:10.1002/2013JA019501

Moskaleva, E.V., and N.Y. Zaalov (2013). Signature of polar cap inhomogeneities in vertical sounding data, Radio Sci., 48, 1-17, doi:10.1002/rds.20060

Nava, B., P. Coïsson, S.M. Radicella (2008), A new version of the NeQuick ionosphere electron density model. Journal of Atmospheric and Solar-Terrestrial Physics, 70(15), 1856-1862 doi:10.1016/j.jastp.2008.01.015

Perrone, L., G. De Franceschi, and T.L. Gulyaeva (2001). The time-weighted magnetic indices ap, PC, AE, and their correlation to the southern high latitude ionosphere, Phys. Chem. Earth, 26(5), 331-334

Reinisch, B. W., and I. A. Galkin (2011), Global ionospheric radio observatory (GIRO), Earth, Planets, and Space, 63, 377-381, doi:10.5047/eps.2011.03.001

Riddolls, R.J. (2006). Technical Memorandum 2006-285, Defence R&D Canada, Ottawa

Saverino, A.L., A. Capria, F. Berizzi, M. Martorella, and E.D. Mese (2013). Progress in Electromagnetics Research B, 50, 97-111

Shepherd, S.G., (2014), Altitude-Adjusted Corrected Geomagnetic Coordinates: Definition and Functional Approximations, J. Geophys. Res., 119, doi:10.1002/2014JA020264

Shubin, V.N., A.T. Karpachev, and K.G. Tsybulya (2013) Global model of the F2 layer peak height for low solar activity based on radio-occultation data, J. Atm. Sol.-Ter. Phys., 104, 106-115, doi:10.1016/j.jastp.2013.08.024

Shubin V.N. (2015), Global median model of the F2-layer peak height based on ionospheric radio-occultation and ground-based Digisonde observations, Adv. Space Res. 56, 916-928, doi:10.1016/j.asr.2015.05.029

Sojka, J.J., R.W. Schunk, W.R. Hoegy, and J.M. Grebowsky (1991), Model and observation comparison of the universal time and IMF By dependence of the ionospheric polar hole. Adv. Space Res. 11(10), 39-42

Thayaparan, T., R.J. Riddolls, and K. Shimotakahara (2016). Proceedings of the 17th International Radar Symposium (IRS), doi:10.1109/IRS.2016.7497370

Themens, D. R., P. T. Jayachandran, R. B. Langley, J. W. MacDougall, and M. J. Nicolls (2013), Determining receiver biases in GPS-derived total electron content in the auroral oval and polar cap region using ionosonde measurements, GPS Solut., 17(3), 357–369, doi:10.1007/s10291-012-0284-6.

Themens, D. R., P. T. Jayachandran, M. J. Nicolls, and J. W. MacDougall (2014), A top to bottom evaluation of IRI 2007 within the polar cap, J. Geophys. Res. Space Physics, 119, 6689–6703, doi:10.1002/2014JA020052.

Themens, D. R., P. T. Jayachandran, and R. B. Langley (2015), The nature of GPS differential receiver bias variability: An examination in the polar cap region, J. Geophys. Res. Space Physics, 120, 8155–8175, doi:10.1002/2015JA021639.

Themens, D.R., and P.T. Jayachandran (2016), Solar activity variability in the IRI at high latitudes: Comparisons with GPS total electron content. J. Geophys. Res. Space Physics, 121, doi:10.1002/2016JA022664.

Titheridge, J. E. (1988), The real height analysis of ionograms: A generalized formulation, *Radio Sci.*, 23(5), 831–849.

Yamazaki, Y., M.J. Kosch, and E.K. Sutton (2015), A model of high-latitude thermospheric density. J. Geophys. Res. Space Phys., 120, doi:10.1002/2015JA021371

Weimer, D. R. (1996), A flexible IMF dependent model of high-latitude electric potentials having "space weather" applications, Geophys. Res. Let., 23, 2549-2553.

Wu, J., and P.J. Wilkinson (1995). Time-weighted magnetic indices as predictors of ionospheric behaviour, J. Atmos. and Solar-Terr. Phys., 57(14), 1763-1770

Xiong, C., H. Lu¨hr, and S.Y. Ma (2013), The subauroral electron density trough: Comparison between satellite observations and IRI-2007 model estimates, Adv. Space Res. 51, 536-544, doi:10.1016/j.asr.2011.09.021

This page intentionally left blank.

List of symbols/abbreviations/acronyms/initialisms

DND	Department of National Defence
E-CHAIM	Empirical Canadian High Arctic Ionospheric Model
IRI	International Reference Ionosphere
NmF2	Peak density of the F2-layer
hmF2	Height of the F2-layer peak
foF2	The F2-layer critical frequency
M3000F2	Ratio of the MUF to foF2
MUF(3000)	Maximum Usable Frequency at 3000km distance
CHAIN	Canadian High Arctic Ionospheric Network
IRTAM	IRI-based Real-Time Assimilative Model
GIRO	Global Ionospheric Radio Observatory
MIT	Main Ionospheric Trough
DRDC	Defence Research and Development Canada
DSTKIM	Director Science and Technology Knowledge and Information Management

DOCUMENT CONTROL DATA

*Security markings for the title, authors, abstract and keywords must be entered when the document is sensitive

1. ORIGINATOR (Name and address of the organization preparing the document. A DRDC Centre sponsoring a contractor's report, or tasking agency, is entered in Section 8.)

University of New Brunswick
3 Bailey Drive
P.O. Box 4400
Fredericton, New Brunswick
Canada
E3B 5A3

2a. SECURITY MARKING (Overall security marking of the document including special supplemental markings if applicable.)

CAN UNCLASSIFIED

2b. CONTROLLED GOODS

NON-CONTROLLED GOODS
DMC A

3. TITLE (The document title and sub-title as indicated on the title page.)

The Empirical Canadian High Arctic Ionospheric Model (E-CHAIM): NmF2 and hmF2

4. AUTHORS (Last name, followed by initials – ranks, titles, etc., not to be used)

Themens, D. R.; McCaffrey, A.M.; Jayachandran, P.T.; Reid, B.

5. DATE OF PUBLICATION (Month and year of publication of document.)	6a. NO. OF PAGES (Total pages, including Annexes, excluding DCD, covering and verso pages.)	6b. NO. OF REFS (Total references cited.)
January 2018	37	41

7. DOCUMENT CATEGORY (e.g., Scientific Report, Contract Report, Scientific Letter.)

Contract Report

8. SPONSORING CENTRE (The name and address of the department project office or laboratory sponsoring the research and development.)

DRDC – Ottawa Research Centre
Defence Research and Development Canada, Shirley's Bay
3701 Carling Avenue
Ottawa, Ontario K1A 0Z4
Canada

9a. PROJECT OR GRANT NO. (If appropriate, the applicable research and development project or grant number under which the document was written. Please specify whether project or grant.)	9b. CONTRACT NO. (If appropriate, the applicable number under which the document was written.)
03ba	W7714-186507/001/SS

10a. DRDC PUBLICATION NUMBER (The official document number by which the document is identified by the originating activity. This number must be unique to this document.)	10b. OTHER DOCUMENT NO(s). (Any other numbers which may be assigned this document either by the originator or by the sponsor.)
DRDC-RDDC-2018-C195	

11a. FUTURE DISTRIBUTION WITHIN CANADA (Approval for further dissemination of the document. Security classification must also be considered.)

Public release

11b. FUTURE DISTRIBUTION OUTSIDE CANADA (Approval for further dissemination of the document. Security classification must also be considered.)

12. KEYWORDS, DESCRIPTORS or IDENTIFIERS (Use semi-colon as a delimiter.)

Canadian High Arctic Ionospheric Model; International Reference Ionosphere; High-Frequency.

13. ABSTRACT/RÉSUMÉ (When available in the document, the French version of the abstract must be included here.)

We present here the Empirical Canadian High Arctic Ionospheric Model (E-CHAIM) quiet NmF2, perturbation NmF2, and quiet hmF2 models. These models provide peak ionospheric characteristics for a domain above 50°N geomagnetic latitude. Model fitting is undertaken using all available ionosonde and radio occultation electron density data, constituting a dataset of over 28 million observations. A comprehensive validation of the model is undertaken and performance is compared to that of the International Reference Ionosphere (IRI).

In the case of the quiet NmF2 model, the E-CHAIM model provides a systematic improvement over the IRI URSI maps. At all stations within the polar cap, we see drastic RMS error improvements over the IRI by up to 1.3MHz in critical frequency (up to 60% in NmF2). These improvements occur primarily during equinox periods and at low solar activities, decreasing somewhat as one tends to lower latitudes. Qualitatively, the E-CHAIM is capable of representing auroral enhancements in NmF2, as well as the location and extent of the Main Ionospheric Trough (MIT), not reproduced by the IRI. The included NmF2 storm model demonstrates improvements over the IRI by up to 35% and over the quiet-time E-CHAIM model by up to 30%.

In terms of hmF2, over the validation periods used in this study, we found overall RMS errors of ~13km for E-CHAIM, with IRI2007 overall hmF2 errors ranging between 16km and 22km. The E-CHAIM performs comparably to or slightly better than the IRI within the polar cap; however, significant improvements are found within the auroral oval.

Dans cet article, nous présentons les modèles de la densité maximale d'ionisation, *N*mF2, de l'ionosphère perturbée et de l'ionosphère calme ainsi que l'altitude de la densité maximale, *h*mF2, de l'ionosphère calme du *Modèle empirique de l'ionosphère du haut arctique canadien* (E-CHAIM). Ces modèles prédisent les caractéristiques maximales de l'atmosphère dans le domaine au-delà du 50e degré de latitude géomagnétique. L'ajustement du modèle a été réalisé à partir de toutes les données disponibles des ionosondes et les densités électroniques obtenues par occultation radio qui, réunies, constituent un ensemble de plus de 28 millions d'observations. Nous avons entrepris une validation exhaustive du modèle et comparé son comportement à celui de l'ionosphère internationale de référence (IIR).

Dans le cas de la *N*mF2 de l'ionosphère calme, le modèle E-CHAIM présente une amélioration systématique par rapport aux cartes de l'IIR de l'URSI. Pour toutes les stations de la calotte polaire, nous constatons, par rapport à l'IIR, des améliorations considérables de l'erreur quadratique de la fréquence critique (jusqu'à 60 % pour la *N*mF2) jusqu'à 1,3 MHz. Ces améliorations sont particulièrement visibles autour de l'équinoxe et pendant les périodes de faible activité solaire, mais diminuent légèrement en s'approchant des latitudes basses. De manière qualitative, le modèle E-CHAIM peut représenter les hausses aurorales de *N*mF2, ainsi que la position et l'étendue du creux ionosphérique principal qui ne sont pas reproduites par l'IIR. Le modèle des tempêtes de *N*mF2 inclus montre des améliorations allant jusqu'à 35 % par rapport à l'IRR, et le modèle de temps calme des améliorations jusqu'à 30 %.

Pour les périodes de validation utilisées lors de cette étude, nous avons constaté des erreurs quadratiques d'environ 13 km pour E-CHAIM, alors que pour l'IRR 2007, les erreurs globales de *h*mF2 se situent entre 16 et 22 km. Le rendement du modèle E-CHAIM est comparable ou légèrement supérieur à celui de l'IIR dans la calotte polaire, mais nous avons constaté des améliorations notables dans l'ovale auroral.